The Journal of Experimental Biology 211, 717-730
Published by The Company of Biologists 2008
doi:10.1242/jeb.012146

Vortex wake and flight kinematics of a swift in cruising flight in a wind tunnel

P. Henningsson[1,*], G. R. Spedding[2] and A. Hedenström[1]

[1]Department of Theoretical Ecology, Lund University, SE-223 62 Lund, Sweden and [2]Department of Aerospace and Mechanical Engineering, University of Southern California, Los Angeles, CA 90089-1191, USA

*Author for correspondence (e-mail: per.henningsson@teorekol.lu.se)

Accepted 2 January 2008

SUMMARY

In this paper we describe the flight characteristics of a swift (*Apus apus*) in cruising flight at three different flight speeds (8.0, 8.4 and 9.2 m s^{-1}) in a low turbulence wind tunnel. The wingbeat kinematics were recorded by high-speed filming and the wake of the bird was visualized by digital particle image velocimetry (DPIV). Certain flight characteristics of the swift differ from those of previously studied species. As the flight speed increases, the angular velocity of the wingbeat remains constant, and so as the wingbeat amplitude increases, the frequency decreases accordingly, as though the flight muscles were contracting at a fixed rate. The wings are also comparatively inflexible and are flexed or retracted rather little during the upstroke. The upstroke is always aerodynamically active and this is reflected in the wake, where shedding of spanwise vorticity occurs throughout the wingbeat. Although the wake superficially resembles those of other birds in cruising flight, with a pair of trailing wingtip vortices connected by spanwise vortices, the continuous shedding of first positive vorticity during the downstroke and then negative vorticity during the upstroke suggests a wing whose circulation is gradually increasing and then decreasing during the wingbeat cycle. The wake (and implied wing aerodynamics) are not well described by discrete vortex loop models, but a new wake-based model, where incremental spanwise and streamwise variations of the wake impulse are integrated over the wingbeat, shows good agreement of the vertical momentum flux with the required weight support. The total drag was also estimated from the wake alone, and the calculated lift:drag ratio of approximately 13 for flapping flight is the highest measured yet for birds.

Key words: swift, *Apus apus*, aerodynamics, flight, wake, kinematics, wind tunnel, digital particle image velocimetry (DPIV).

INTRODUCTION

When an animal flies through the air it leaves behind a region of modified fluid motions, known collectively as a wake, which reflects the magnitude and time history of aerodynamic forces generated by the wings and body. Newton's third law requires that the forces exerted by a solid body upon a surrounding fluid be exactly equal and opposite to the forces exerted by the fluid on the body, and studying the wake is an elegant practical method for examining the forces produced with minimal interference with the flying animal. In principle, the consequences of all wing, tail and body actions are to be found in the wake. In steady motions, the flow fields responsible for lift generation of an aerofoil can conveniently be characterized by the strength and geometry of compact regions of shear and rotation, idealized mathematically as line vortices. Then a description of the wake vorticity is entirely sufficient for quantitative description and prediction of the forces on the body. As Dabiri (Dabiri, 2005) [summarized in Peng and Dabiri (Peng and Dabiri, 2008)] has recently stressed, in unsteady flows there can be another significant component of the force that appears as an acceleration of the line vortices themselves. The accelerating component itself does not have vorticity, but is a purely potential flow, and both types of flowfield need to be measured in order to account for all forces acting on the fluid. In many cases of moderate amplitude flapping animal flight, however, it is likely that the unsteady accelerations of the vortices themselves are comparatively small compared with the rotational acceleration of the fluid around them. We will return to this point later but, for now, we will consider the wake vorticity as the primary and important distinguishing characteristic of wakes in animal flight.

Idealized vortex wake models have been developed describing wakes found at different flight speeds. The discrete loop wake (Rayner, 1979a; Rayner, 1979b; Rayner, 1979c) postulates that during each downstroke a single vortex loop is formed and shed, and the resulting momentum flux provides the force required to support the weight and overcome viscous and induced drag forces. In this model the upstroke is considered inactive. This model corresponds well (at least qualitatively) to the wakes found in slow forward flight of small passerines, pigeons and jackdaws (Kokshaysky, 1979; Spedding et al., 1984; Spedding, 1986; Spedding et al., 2003b). At higher, cruising flight speed a model different from the discrete loop model was found to be a better approximation of the wake. This model is called the constant circulation model (Spedding, 1987; Rayner et al., 1986) and approximates the wake disturbance as a pair of trailing wingtip vortices of nearly constant circulation that undulate up and down, roughly following the wingtip trace. In this case both down- and upstroke are active, where the downstroke produces lift and thrust and the upstroke produces lift and negative thrust (drag). Because the wings are flexed during the upstroke, the aerodynamic forces are smaller in magnitude, and the resulting net horizontal force is the thrust. An interesting characteristic of this wake model is that since the circulation of the wake vortices does not change, then neither can the wing circulation, and so there is no large-scale shedding of spanwise vorticity during the wingbeat cycle. This would appear, but has never been proven, to be an efficient form of locomotion.

A third type of wake, called the ladder wake, has been proposed for animals that fly with rigid, relatively inflexible wings, such as

humming birds and swifts (Pennycuick, 1988; Pennycuick, 1989). As noted above, for animals flying with upstroke wing flexion, the net forward thrust is achieved by an asymmetry in the effective span of the downstroke and upstroke. If the wings do not flex, then positive thrust must be achieved by some other means. The ladder wake model provides the required asymmetry by variation of circulation, rather than wake width. As with the constant circulation wake, the wings leave continuous trailing wingtip vortices, but in this case they are connected by spanwise vortices shed during both wingbeat turning points. At the transition from the upstroke to the downstroke a distinct vortex with positive (counter-clockwise) circulation is shed from the wings as the circulation of the bound vortex on the wings increases. Then, at the transition from downstroke to upstroke, the wing circulation decreases and so a corresponding vortex with negative (clockwise) circulation is shed. The upstroke–downstroke asymmetry required for net thrust comes from the different circulation values. The ladder wake has been proposed but never observed, perhaps because no equivalent wake studies have been made of comparatively rigid-winged birds.

Studies of birds and bats in wind tunnel flight show that real wakes differ from these idealized wake models (Spedding et al., 2003b; Hedenström et al., 2006a; Hedenström et al., 2007; Rosén et al., 2007). In this paper we investigated the wake properties of the swift *Apus apus* L., since it has been suggested as a candidate species for the ladder wake. The swift is unlike most bird species, with respect both to its biology and to its body design. It spends almost its entire lifetime on the wing, day and night, landing only to breed (Lack, 1956) and only occasionally roosting in trees (Holmgren, 2004). This extreme lifestyle is naturally coupled to a specialized body and wing design. The swift has a streamlined body and long, relatively slender, aft-swept wings. This design and its aerodynamic function potentially contain features that, if understood, would widen our knowledge of animal flight.

MATERIALS AND METHODS

The wind tunnel

Experiments were performed in the low turbulence wind tunnel at Lund University, Sweden. The wind tunnel has an octagonal test section, 1.22 m wide and 1.08 m high. The 1.2 m upstream part of the test section, where the actual measurements are performed, has Plexiglas walls and the 0.5 m downstream part is open, providing quick and easy access to the flying animal during experiments. The air speed across 97.5% of the test section is within ±1.3% of the mean and the turbulence level in the upper test section part is on average 0.04% of the wind speed (Pennycuick et al., 1997). The *x*-, *y*- and *z*-axes of a rectangular coordinate system lie in the streamwise, spanwise and vertical directions, respectively.

Birds, housing and flight training

Two juvenile swifts were captured on 2nd August, 2006, in their nest, the day before their expected fledging. The timing of capture was decided based on cues such as restlessness and intense flight muscle training inside the nest boxes. The birds were then kept for 12 days and during this time, when not flying in the wind tunnel, they were kept in a lidless plastic box with a nest bowl. They were hand fed with a mixture of maggots, crickets, dried insects and supplementary vitamin powder for birds every second hour throughout daytime. The mass and overall health status of the birds were monitored carefully. The flight training required was minimal and both birds made their premier flight in life in the wind tunnel the day after capture with impressive success. The birds quickly learned to fly stably in the test section, within the first 2 days of training. The birds were guided in the tunnel by a marker (a fly on a string suspended from the ceiling) upstream and to the side of the measuring volume. One of the birds, however, started to fly into the contraction section upstream of the test section and could therefore not be used for quantitative measurements, but for visual observation only. Both birds were released into the wild with normal body weights and in good condition on 13th August, 2006. Morphological details of the single bird used in the experiments are presented in Table 1.

Wingbeat kinematics

Flight kinematics of the swift were recorded in the wind tunnel using a high-speed camera (NAC Hotshot 1280, Simi Valley, CA, USA) filming from a posterior position, *ca* 1.2 m downstream of the test section to ensure negligible disturbance of the flow in the test section. The camera recorded sequences of 2.75 s in duration at 60 frames s^{-1} and with an exposure time of 1/60 s. The sequences were recorded as 24 bit grayscale AVI-files with a resolution of 640 pixels×510 pixels and a pixel aspect ratio of 1:1. The swift was filmed in steady flight at three wind speeds at which the bird was found to be able to fly in a natural manner: 8.0, 8.4 and 9.2 m s^{-1}. Numerous sequences were initially recorded for each wind speed (in total N=460) and then each sequence was carefully and critically studied so only sequences or parts of sequences showing perfectly stable flight and where both the upper and the lower wingtip turning points could be seen were used for further analysis (N=7, 12 and 6 for 8.0, 8.4 and 9.2 m s^{-1}, respectively).

For each of the remaining sequences the position of the shoulder joint and the wingtip in each frame were digitized in a custom-written MatLab program (The MathWorks, Inc., Natick, MA, USA), recording the *ix*- and *iy*-position (in camera pixel coordinates) of these two reference points, respectively ($p1$, $p2$ in Fig. 1). The horizontal camera axis was aligned with the mean flow in the wind tunnel, and on corresponding reference grids. The position of the shoulder joint was in every sequence clearly distinguished, while for the wingtip, moving much more rapidly, the blur sometimes prevented accurate positioning. In these cases the position of the wingtip was interpolated from a cubic smoothing spline function to the total vector of positions for the sequence. To calculate the amplitude and the wingspan in real coordinates (m), a reference length was determined by finding the time of the upper turning point in each wingbeat and calculating the length between the shoulder joint and wingtip in pixels at this moment. Turning points are the transitions from down- to upstroke and *vice versa* and were found from the locations of zero derivatives of the spline-fitted time series of shoulder-to-tip angles. At the upper turning point of the wingbeat the swift's wing is completely outstretched and gives an accurate reference length. The measured length (m) of the swift wing (shoulder–wingtip; Table 1) was divided by the mean of the distances in pixels to obtain a conversion factor, unique for every sequence.

Table 1. Morphological details of the bird used in the experiment

Total mass (kg)	0.039
Wingspan (m)	0.38
Wing area[a] (m^2)	0.015
Aspect ratio[b]	9.6
Shoulder–wingtip (m)	0.1789
Body frontal area (m^2)	0.0017

[a]Defined as the area of both wings including the body area in between.
[b]Defined as wingspan squared divided by wing area.

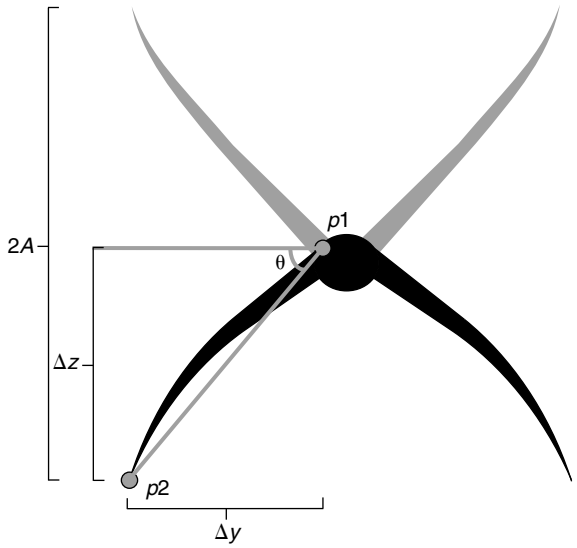

Fig. 1. Rear view of the flying swift showing the method of digitizing from high-speed films. The shoulder joint (*p*1) and wingtip (*p*2) are located and with the measurements of distance in the horizontal (Δy) and vertical (Δz) direction between these, the stroke angle (θ) can be calculated. The peak-to-peak amplitude, 2*A*, is the distance between the wingtip at the upper and lower turning point.

The uncertainty in estimating wing marker positions is determined by the pointing accuracy of the human operator and by the discretization of the data in space and time. The wingbeat frequency was around 9 Hz and the framing rate was 60 Hz. The relatively coarse temporal resolution is why smooth functions were fitted to the data before analysis. Note that measurements such as semispan and wingtip amplitude are not necessarily systematically underestimated because the spline fitting function is as likely to overshoot the data as to underestimate it. Overall uncertainties in the kinematic data may be estimated to be less than 5%.

From each digitized sequence the following kinematic data were derived.

Wingbeat frequency (*f*): the wingbeat frequency was derived from the angle between the shoulder joint and the wingtip, which was calculated for each frame in each flight sequence (Fig. 1). The sequence of angles was used as a signal from which the dominant frequency was derived using a discrete Fourier transform. A dominant frequency was distinct in every sequence analysed and the mean of these was calculated.

Wingbeat angular amplitude (θ_{tot}): the total wingbeat angular amplitude was calculated by recording the absolute angle between the shoulder joint and the wingtip at the turning points of the wingbeat. The upper and lower angles are added to yield the peak-to-peak angular amplitude in each wingbeat cycle ($\theta_{tot}=\theta_u+\theta_l$), and a mean was calculated for each sequence (Fig. 1).

Wingbeat amplitude (2*A*): the peak-to-peak wingbeat amplitude was calculated from the absolute distance in *z* between the shoulder joint and the wingtip (Fig. 1), for both upper and lower wingtip excursions ($2A=A_u+A_l$). The mean of the measured amplitude of each wingbeat for the complete sequence was calculated.

Wingbeat angular velocity ($\dot{\theta}_{u,d}$): the angular velocity during mid-upstroke and -downstroke was derived from the derivative of the spline function of the angular time series. The mid-stroke was defined as the moment at which the angle between the shoulder joint and the wingtip was zero, i.e. when the wing was passing the horizontal plane with respect to the shoulder joint. The mean angular velocities during mid-upstroke ($\dot{\theta}_u$) and -downstroke ($\dot{\theta}_d$) were calculated for each sequence.

Downstroke duration and fraction (T_d, τ): the downstroke duration, T_d, was defined as the time for the wing to travel from the upper turning point to the lower one. The downstroke fraction was $\tau=T_d/T$, where T is the period of one entire wingbeat cycle.

Wing semispans (b_d,b_u) and span ratio, (R): the local semispan in each frame was measured by multiplying the absolute distance in the horizontal direction from the shoulder joint to the wingtip in pixels by the conversion factor described above, and adding half the body width to the result. As with the mid-stroke angular velocity, $\dot{\theta}_{u,d}$, the mid-stroke span was calculated when the wing passed through the horizontal plane. The semispan is therefore defined as the horizontal component of the distance between the body centreline and wingtip. This is the length that best approximates the aerodynamically significant quantity. The span ratio was calculated as the ratio between the semispans at mid-upstroke and -downstroke, $R=b_u/b_d$.

Flow visualization

The method of quantitative flow visualization is a custom variant of digital particle image velocimetry (DPIV) known as CIV, as presented in Spedding et al. (Spedding et al., 2003a). A thin fog (particle size 1 μm) is continuously introduced downstream of the test section and re-circulates in the tunnel until evenly distributed. During measurements, the fog is illuminated by a double-pulsed laser (Spectra Physics Quanta Ray PIV II, dual head Nd:YAG, with Q-switch-controlled 200 mJ per pulse energy) at a repetition frequency of 10 Hz. The laser produces a 3 mm thick vertical light sheet, aligned with the flow, entering from beneath the test section floor. The time between pulse pairs is controlled by a delay generator (Stanford Research System DG535) that can be set to introduce an arbitrary time delay, δt. For any given flow speed, δt was tuned carefully to allow the maximum possible mean particle image displacement without losing data from complex parts of the flow. A CCD array camera (Redlake, Megaplus II ES 4020, Tallahassee, FL, USA), with focal plane positioned parallel to the laser sheet, captures images in synchrony with the pulsed laser. The camera is operated in binning mode (1024 pixels×1024 pixels) and the images are transferred via a digital interface (DVR Express 1.23, IO Industries, London, ON, Canada) to a parallel SCSI disk array on a PC, where CIV processing takes place.

Calculated displacements of rectangular windows in the pixel image plane are converted to velocities in the plane of the laser sheet, using a pixel conversion factor and the known time δt. The laser sheet is always oriented vertically and streamwise, so the velocity components are $\{u,w\}$ in $\{x,z\}$. The wake structure is described in terms of the spanwise component of vorticity:

$$\omega_y = \frac{\partial w}{\partial x} - \frac{\partial u}{\partial z}.$$

In a well-run experiment, uncertainties in $\{u,w\}$ of 1–2% are realizable, which typically gives uncertainties in gradient quantities of ±5–10%.

A rear-view camera (described above) is positioned downstream of the test section recording film sequences used for classifying the position of the bird with respect to the laser. The position of the bird in relation to the light sheet was classified discretely as, first, left wing (L), right wing (R) or body (LR) and, second, as inner wing (X), mid-wing (Y) or outer wing (Z). For example, an image

corresponding to the inner left wing would be denoted as 'LX' (Fig. 2). The bird typically flew 0.4 to 0.5 m upstream of the laser sheet, which resulted in a small time delay between the motion recorded by the downstream camera and the wake images recorded by the PIV camera. When flight speed U=8.4 m s^{-1}, the delay would be around 0.05 s. This is compensated for by linking the wake images to positions of the bird in the high-speed camera two to three frames before the laser flashes occur.

Force balance

For a bird to fly level, the vector sum of thrust and lift must be equal to the vector sum of drag and the weight. It is convenient to analyse the wake by comparison with two idealized wake models, one at each end of a spectrum of possible intermittency. The first model describes the wake as a discrete shedding of vortex loops during each downstroke. In this intermittent model the upstroke is inactive and leaves no wake signature (Spedding et al., 2003b). The projected area of an elliptical vortex loop is:

$$S_e = \pi b \frac{\lambda_d}{2}, \quad (1)$$

where b is the wing semispan (m) and λ_d is the downstroke wavelength (the length travelled in a streamwise direction during the downstroke). The vertical impulse, I_z, contained in the structure is the product of its area and the circulation:

$$I_z = \rho S_e \Gamma_1, \quad (2)$$

where ρ is the air density and Γ_1 is a reference circulation that is sufficient to support the weight for one wingbeat period T, from a single elliptical loop with area S_e. This can be readily calculated as:

$$\Gamma_1 = \frac{WT}{\rho S_e}, \quad (3)$$

where W is body weight. The second model, found at the other end of the intermittency spectrum, is a 'power-glider'. A rectangular wake is continuously extended at speed U, and over an interval T it grows by $UT\times 2b$. The reference circulation required for weight support in this case is thus:

$$\Gamma_0 = \frac{W}{\rho U 2b}. \quad (4)$$

The reference circulations Γ_0 and Γ_1 are likely to bracket the actual circulation values in the real wake. Γ_0 would be the minimum circulation required if the bird had to do no work against drag, and the flat, rectangular wake were to provide only weight support. Γ_1 would be the value required if only the downstroke were active and all the momentum flux for lift (ignoring drag) had to be produced during the downstroke alone.

RESULTS

Wingbeat kinematics

A total of 25 high-speed film sequences at three different flight speeds were obtained, 8.0 m s^{-1} (N=7), 8.4 m s^{-1} (N=12) and 9.2 m s^{-1} (N=6) containing 30, 30 and 20 complete wingbeats, respectively. Even though the range of flight speeds was quite narrow, the wingbeat frequency of the swift showed a clear decrease with increasing flight speed, dropping from 9.1 to 8.3 Hz (Fig. 3A). The shoulder-to-wingtip angle, θ_u, of the wing at the upper turning point increased with flight speed, while the angle at the lower turning point, θ_d, did not (Fig. 3B). The downstroke duration, T_d, increased with increasing flight speed (Fig. 3D), but the angular velocity of both the up- and downstrokes, $\dot{\theta}_{u,d}$, did not vary greatly (Fig. 3E). The downstroke fraction (τ, Fig. 3D), down- and upstroke semispans (b_d, b_u, Fig. 3F), and consequently span-ratio (R, Fig. 3F) also all remained approximately constant across U.

The primary change in observed wingbeat kinematics with increasing flight speed was an increase in wingbeat amplitude. Since the measured wing angular velocity remained approximately constant, the result was a decrease in observed flapping frequency.

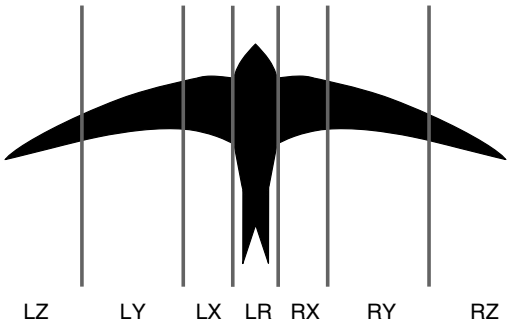

Fig. 2. The discrete classification system and notation. The LR position corresponds to the body, X is the arm section of the wing, and Y and Z are the inner and outer parts of the hand wing, respectively.

Wake velocity and vorticity fields

The wingbeat frequency of the swift at the flight speed examined (8.4 m s^{-1}) was 8.6 Hz, with wake wavelength $\lambda=UT$= 8.4/8.6=0.98 m. Each frame recorded by the PIV camera covers only 0.2 m in x, so approximately five full frames were needed to cover a complete wingbeat. The recording frequency of the camera is 10 Hz and with the swift wingbeat frequency, f=8.6 Hz, sequences of progressively decreasing phase of the wingbeat were obtained. Images were phase-ensembled to reconstruct the representative wake of a complete wingbeat at each spanwise position on the wing in Fig. 4. Since the swift flies between 0.4 and 0.5 m upstream of the laser sheet, the wake was sampled approximately 10 chord lengths away from its physical origin at the wings and body.

Steady flapping flight

Fig. 4A–C shows the wake shed behind the wings during one complete wingbeat cycle at three positions, moving from inner (Fig. 4A) to outer wing (Fig. 4C). All three sections show that vorticity of predominantly positive sign is shed during the downstroke, and that this changes to vorticity of mostly negative sign during the upstroke. The amplitude of the vertical excursions of the wake increases from base to tip (Fig. 4A–C) of the wing, as one would expect. The patterns of shed vorticity and associated velocity vectors on the upstroke of the outer wing section (Fig. 4C) are more complex than further inwards.

The uniformity in sign and gradual change in strength of the shed vorticity are quite different from those of previously studied birds at moderate-/high-speed flight. When combined with the absence of any large-scale spanwise structure at the turning points, the shed wake vorticity implies a time-history of circulation change on the wing itself that is also gradually and constantly changing. During the downstroke, the circulation on the wing increases to reach a maximum at, or just before, the lower turning point. The circulation

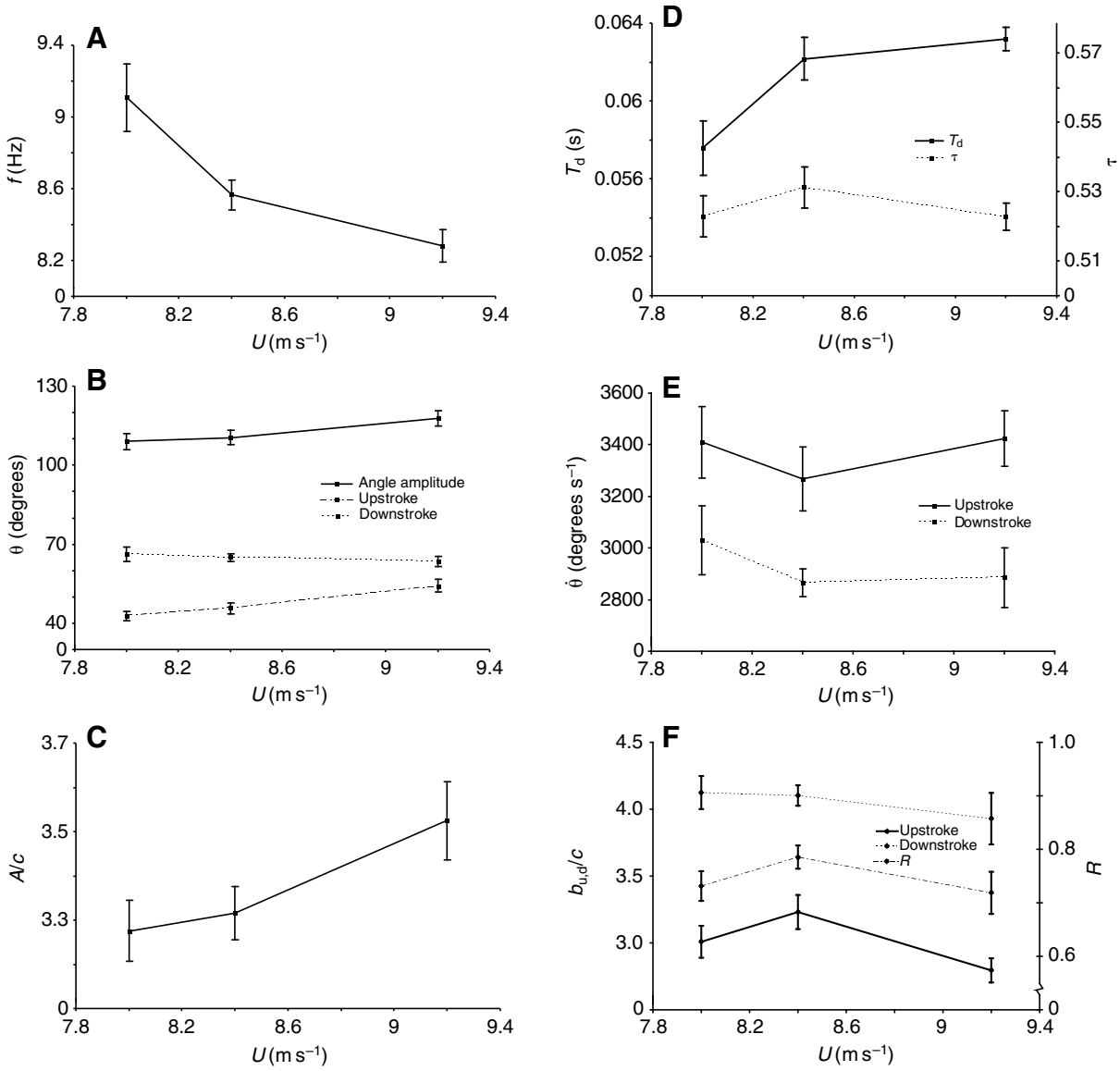

Fig. 3. (A) The wingbeat frequency, *f*, decreases with increasing flight speed, *U*, from 9.1 Hz at 8.0 m s^{-1} to 8.3 Hz at 9.2 m s^{-1}. (B) Upper (u), lower (d) and total (tot) angular excursion, θ, of the wing in the vertical plane as a function of flight speed, *U*. The increase in $\theta_{tot}(U)$ comes only from the increase in $\theta_u(U)$. (C) Amplitude, *A*, normalized by mean chord length, *c*. (D) The downstroke duration, T_d, increases with flight speed, *U*. The downstroke fraction, τ, does not vary with flight speed, *U*. (E) The wing angular velocity at mid-upstroke and -downstroke, $\dot{\theta}_{u,d}$, does not vary greatly with flight speed, *U*. (F) Wing semispans, $b_{u,d}$ at mid-upstroke and -downstroke normalized by mean chord length (*c*) *vs* flight speed, *U*. Wing semispan does not vary with flightspeed. The span ratio, *R*, does not change with flight speed, *U*. Error bars represent ±s.e.m.

then gradually decreases again during the upstroke. At the end of the upstroke, the shed vorticity is weakly negative, and the magnitude of the associated induced velocity field in the vicinity is also weak.

The direction and magnitude of the induced velocity field (we presume it is a global flow that can be thought of as being caused by the compact vortices in the wake) is consistent with a downwash from a wing that is lifting throughout the wingbeat, but the lift and thrust on the downstroke are stronger than the lift and drag on the upstroke. The net positive thrust propels the bird forward.

Interpreting three-dimensional vortex structure from stacks of two-dimensional velocity fields can be arduous, but certain checks are also possible. For example, wingtip trailing vortices should induce a downwash between them (as noted above) but should also be associated with an upwash in the outer wake, as the airflow is swept from high to low pressure around the wingtips. This is seen in Fig. 5. These characteristics of wingtip vortices are found in all phases of the wingbeat.

Body drag

The most prominent feature of the body wake (Fig. 4D) is a mean flow from right to left (towards the bird's body). A velocity profile in this direction is commonly called a velocity defect, since it is a region where the local flow speed is lower than ambient. It is lower because friction between the body and the mean flow reduces the local flow speed, and consequently exerts a drag force on the body. Although there is a region of significant downwash towards the end of the downstroke and the beginning of the upstroke, it is notable that the body wake was modulated only weakly by the induced flow of the lifting wings further away from the centreline. The wake and

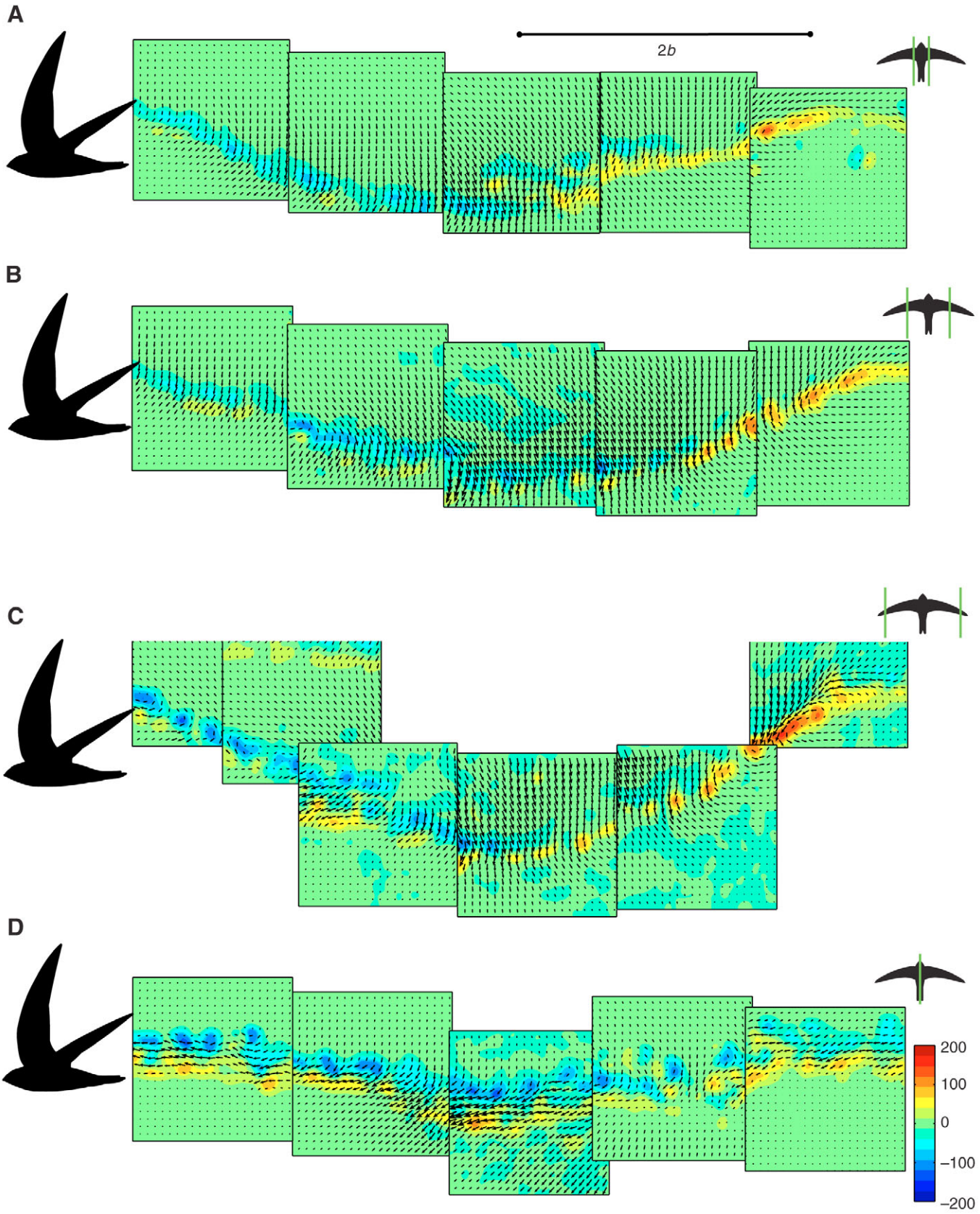

Fig. 4. Reconstruction of the vortex wake from a complete wingbeat at different spanwise locations: (A) arm wing (X in Fig. 2), (B) mid-hand (Y in Fig. 2), (C) outer-hand (Z in Fig. 2), and (D) body (LR in Fig. 2). The mean flow has been subtracted so the reference frame is in still air, as though the bird has passed from right to left. The spanwise vorticity, $\omega_y(x,z)$, is colour coded on a constant scale, symmetric about 0 s^{-1}. Velocity vectors are drawn with 1/3 of the actual density.

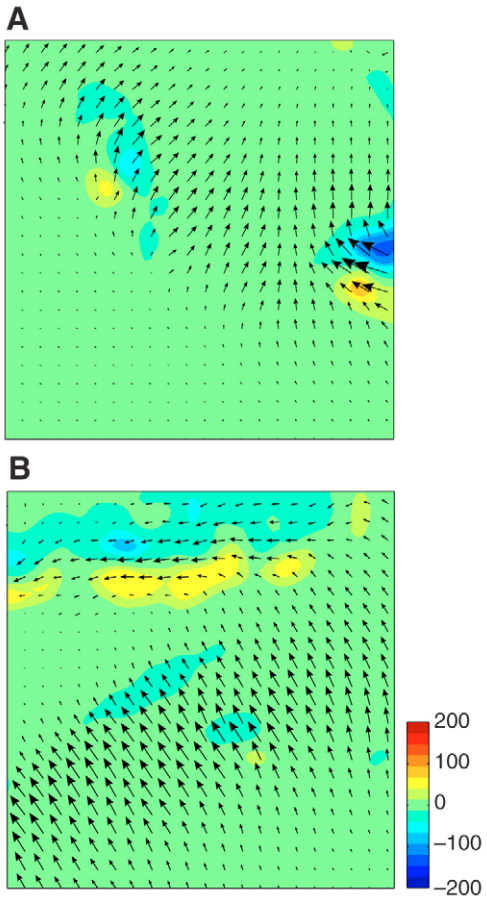

Fig. 5. $\omega_y(x,z)$ for outboard cuts through the edge of wingtip vortices on the upstroke (A) and downstroke (B).

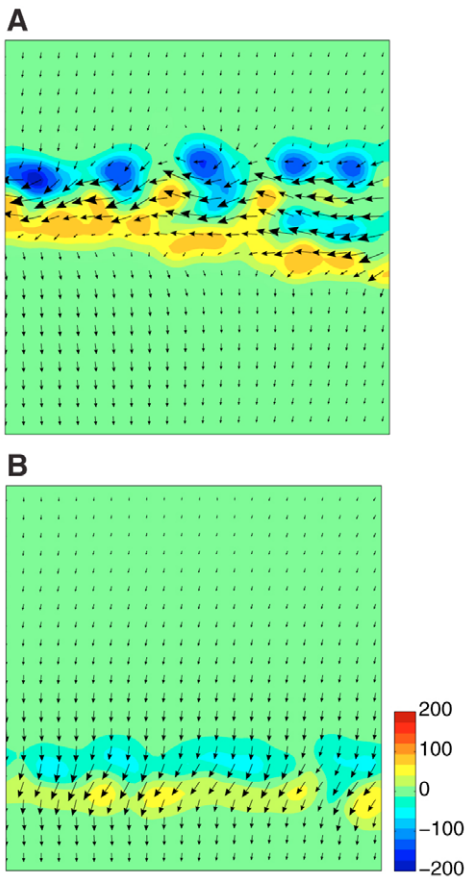

Fig. 6. $\omega_y(x,z)$ for wakes generated during short gliding phases: (A) body (LR in Fig. 2) and (B) mid-hand (Y in Fig. 2).

induced downwash of the two wings has not merged across the body, whose drag component still persists, even at x/c=10.

The velocity defect was accompanied by chains of opposite-signed patches of vorticity, but we cannot say whether these were shed at the body or whether they developed as free shear-layer instabilities in the wake. Similarly, the possible contribution of the tail towards the wake structure is not easily ascertained. While the tail area is reduced in stable, steady, level flight, small control movements, and their subsequent wake signature, cannot be ruled out.

Gliding flight

A small number of individual frames showed a wake generated during brief, intermittent gliding phases. The central velocity defect behind the body in Fig. 6A is not unlike that seen behind the body in flapping flight, but the far field is much more regular, with a weak global downward flow. The mid-wing section in Fig. 6B is dominated by a global downward motion, which can be predicted as a consequence of lift on the wings. The downflow is deflected slightly to the left, and associated with strips of opposite-signed spanwise vorticity. This local defect profile must come from the friction drag on the wing section.

Quantitative wake analysis

Fig. 4 shows that the wake of the swift consists of almost continuous shedding of wake vortices throughout the wingbeat, implying that the strength of the circulation on the wing, the bound vortex, is also changing continuously. The phenomenon can be quantified, and U=8.4 m s^{-1} can be used as an example. The circulation at different phases of the wingbeat was measured by splitting the data at each spanwise location into five discrete phases of the wingbeat: phase 1 is the end of the upstroke; phase 2 is mid-upstroke; phase 3 is the lower turning point between down- and upstroke; phase 4 is mid-downstroke; and phase 5 is the beginning of the downstroke. Frames were sorted by phases that correspond to a tiling, from left to right, of subwindows covering the ensemble velocity fields such as those shown in Fig. 4. The results appear in Fig. 7A–D. The circulation deposited into the wake in each phase matched a change of circulation of the bound vortex on the wing, with positive wake circulation corresponding to an increase in wing circulation magnitude and negative wake circulation implying a decrease. At all four locations, from body to wingtip, the downstroke is dominated by positive circulation and the upstroke was dominated by negative circulation, consistent with the idea that absolute circulation in the bound vortex accumulates during the downstroke and diminishes during the upstroke. At each location, the maximum positive wake circulation occured at mid-downstroke (phase 4) and the strongest negative circulation occured at mid-upstroke (phase 2).

The peak positive circulations at phase 4 (mid-downstroke) in panels A–C of Fig. 7 all have similar values, suggesting that the circulation variation along the wing was small. The positive wake circulation dropped sharply in the transition from phase 4 to phase 3, over the second half of the downstroke. This was followed by the most rapid rise in negative circulation (at all spanwise locations)

from phase 3 to phase 2, the beginning of the upstroke. The wake behind the outer wing (Fig. 7B,C) had a higher increase in negative circulation than the inner wing (Fig. 7A). Although the relatively unflexed wing appeared to remain aerodynamically active during the upstroke, the outer wing appeared to be more lightly loaded.

The body–tail-generated drag wake (Fig. 7D) had a higher strength cross-stream vorticity than the wing sections. Variation of circulation magnitude with phase similar to that for the wing sections was seen, but the amplitude of the variation was much less. Alongside the observed undulation of the centreline wake (Fig. 4D), the data suggest a coupling of some kind between the body wake vortices and the spanwise vorticity shed from the wing. The data are too far downstream of the body to say more.

The continuous shedding of vorticity into the wake means that no distinct starting or stopping vortices are identifiable, at any point in the wake. In the Introduction, Γ_0 and Γ_1 were introduced as likely limiting values of the wake circulation strengths for wakes composed of rectangular wakes (Γ_0) or discrete, pulsed loops (Γ_1). In practice, however, although the swift generates a wake that might most closely be approximated by a constantly growing rectangular area, the most coherent and strongest vortices could well be trailing wingtip vortices, whose properties are not readily measured in streamwise slices. Fig. 8 shows that the peak circulation of the strongest patches of spanwise vorticity were always significantly less than either reference circulation value. In fact, the strongest vortices were those associated with the body wake. In summary, there were no abrupt changes in circulation on the wing that make it possible to construct a meaningful discrete vortex model of the wake, given the measurements available. We must therefore search for an alternative.

DISCUSSION

Flight characteristics

Both swifts in this study were juveniles and their first flight in the wind tunnel was also their first flight in life. Juvenile swifts leaving their nests must be prepared for constant, day-and-night flight from the moment they drop over the edge. They exercise their flight muscles in the nest prior to fledging, but have no chance to practice the actual technique of flying (Lack, 1956). This could potentially be an explanation for why the swifts of this study so quickly learned to fly in the wind tunnel. Their capacity for controlled and stable flight was the most obvious difference compared with descriptions of other species presented in previous studies, which normally have required lengthy training prior to the actual experiments (e.g. Park et al., 2001; Spedding et al., 2003b; Hedenström et al., 2006a; Rosén et al., 2007). The next obvious difference was the extremely narrow

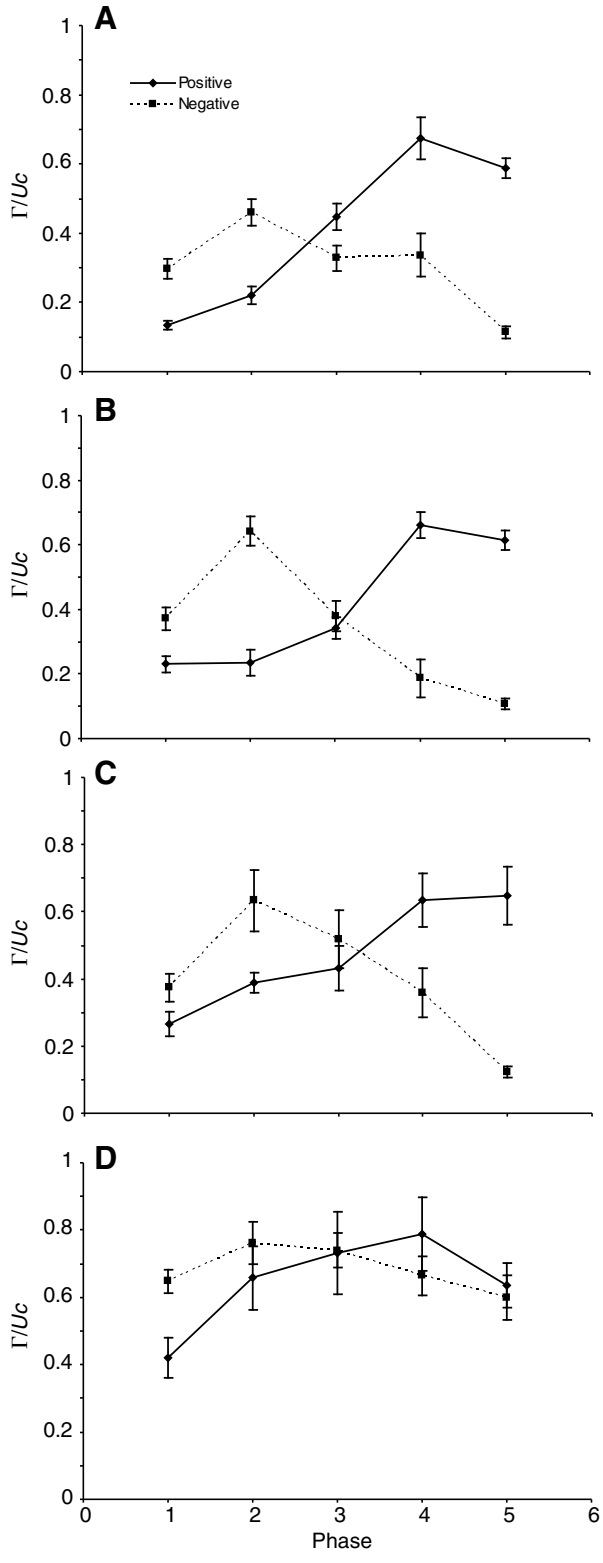

Fig. 7. Normalized total circulation in each phase of the wingbeat, where phase 5 at the right of the abscissa is the beginning of the downstroke and phase 1 at the left marks the end of the upstroke: (A) inner wing (X in Fig. 2), (B) mid-hand (Y in Fig. 2), (C) outer-hand (Z in Fig. 2) and (D) directly behind the body (LR in Fig. 2). Error bars represent ±s.e.m.

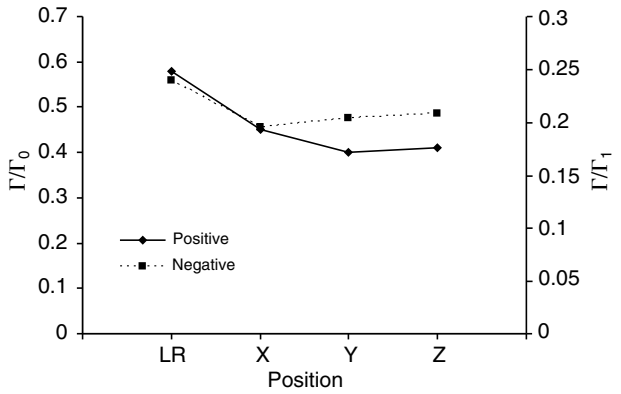

Fig. 8. Maximum observed circulation of any coherent structure in the swift wake relative to two reference circulations, Γ_0 and Γ_1, for the power-glider and pulsed ring generator, respectively. On the abscissa, LR to Z are positions given in Fig. 2.

range of speeds at which the birds would fly. Below approximately 7.5 m s^{-1} the birds seemed unable to sustain stable flight, but dropped to the floor of the test section within a few seconds. A swift flying relaxed and at a natural flight speed flies with its feet held up close to the body and completely tucked in under the feathers (P.H., unpublished obervation). When the swifts of this study were exposed to airspeeds from 7.5 to 9 m s^{-1} this was the case, but when the wind speed exceeded 9 m s^{-1} the feet were extended, indicating that the flight speed was in some way troublesome. The range of natural flapping flight speeds for swifts may be narrow compared with those of other similar-sized bird species.

Wingbeat kinematics

The swift beats its wings at a similar angular velocity at each flight speed. The only direct response to the higher flight speed is an extension of the wingbeat by increasing the shoulder-to-wingtip angle of the upper turning point, resulting in increased wingbeat amplitude. Since the angular velocity does not vary significantly, the downstroke duration, T_d, increases. In the case of the swift, T_d always exceeds T_u, in contrast with findings for passerines where $T_u > T_d$ (e.g. Rosén et al., 2007; Hedenström et al., 2006a; Rosén et al., 2004; Park et al., 2001). The barn swallows of Park et al. (Park et al., 2001) increased their flight speed by increasing angular velocity and decreasing T_d over 8–9.2 m s^{-1}. The curve of $f(U)$ was quadratic over the entire range of flight speeds (4–14 m s^{-1}) with a minimum close to 9 m s^{-1}, but around this minimum (7–11 m s^{-1}) f varied little. A study on robins (*Erithacus rubecula*) showed that the wingbeat frequency and wingbeat amplitude increased slightly (although statistically insignificantly) with increasing flight speed (Hedenström et al., 2006a). A house martin (*Delichon urbica*) showed, like the swift, a decrease in wingbeat frequency with increasing flight speed, but a decreasing downstroke duration (Rosén et al., 2007). The rufous hummingbird (*Selasphorus rufus*) adapts to increasing U in a wind tunnel by varying both amplitude and wing angular velocity, keeping f almost constant at 42 Hz (Tobalske et al., 2007).

The wingbeat frequency measured for this swift ranged from 8.3 to 9.1 Hz, overlapping a predicted value of 8.9 Hz from a semi-empirical relationship derived by Pennycuick (Pennycuick, 1996) as:

$$f = m^{3/8} \boldsymbol{g}^{1/2} b^{-23/24} S^{-1/3} \rho^{-3/8} , \quad (5)$$

where m is the mass of the bird, $\boldsymbol{g}$ is the gravitational acceleration, b is the wingspan, S is the wing area and ρ is the air density. Variable values were based on the morphology of this specific bird (see Table 1) and ρ=1.19 kg m^{-3}. These f values are slightly higher than those derived from the radar studies of Bäckman and Alerstam (Bäckman and Alerstam, 2001; Bäckman and Alerstam, 2002), who found a frequency range of 7.0 to 8.3 Hz, and Bruderer and Weitnauer (Bruderer and Weitnauer, 1971), who observed a range of 6 to 8 Hz.

The span ratio, R, was higher in the swift compared with that in previously studied species in the wind tunnel. It did not change significantly with flight speed but remained at approximately 0.7. Hence, the swift flexes its wings relatively little during the upstroke, which is consistent with visual observation of swifts in free flight (P.H., unpublished observations). Over the same range of absolute flight speeds, $0.2 \leqslant R \leqslant 0.3$ for the barn swallow (Park et al., 2001), R=0.4 for the thrush nightingale (Rosén et al., 2004), R=0.4 for the robin (Hedenström et al., 2006a) and R=0.3–0.4 for the house martin (Rosén et al., 2007). From data on mid-downstroke and -upstroke wingspan presented in Tobalske et al. (Tobalske et al., 2003), estimates of span ratios for ringed turtle doves (*Streptopelia risoria*), budgerigars (*Melopsittacus undulatus*), cockatiels (*Nymphicus hollandicus*) and black-billed magpies (*Pica hudsonia*) can be derived. Span ratios at 9 m s^{-1} for these birds were approximately 0.6, 0.5, 0.4 and 0.3 for the ringed turtle doves, the budgerigars, the cockatiels and the magpies, respectively. The rufous hummingbird of Tobalske et al. (Tobalske et al., 2007) reduces R from 0.98 at U=0 m s^{-1} to 0.9 at U=12 m s^{-1}, and so while the hummingbird also has relatively little wing flexion on upstroke, the opposing trend of $R(U)$ cautions against generalizing the swift results to all rigid-winged birds.

Wake topology

The swift wake shows no obvious similarities to the ladder wake even though the swift has been proposed to be a candidate for this wake type (Pennycuick, 1988; Pennycuick, 1989). The ladder wake model supposes that the circulation changes abruptly between down- and upstroke with the shedding of a distinct vortex in each of the upper and lower turning points, but this was not found in the swift. The wake shows both similarities and differences compared with those of previously examined passerine species.

The continuous shedding of spanwise vorticity is similar to the wake structure of the thrush nightingale, robin and house martin in cruising flight (Spedding et al., 2003b; Hedenström et al., 2006a; Rosén et al., 2007), but here the change in sign is much more regular and systematic (Fig. 4), with positive vorticity shed on the downstroke, transitioning to negatively signed vorticity in the trailing wake from the upstroke. The transition is gradual, with its mid-point at the lower turning point. As an example, the contrasting spatial variation of net wake circulation in the swift and thrush nightingale is shown in Fig. 9. The thrush nightingale circulations at both medium and high flight speeds are relatively sharply peaked at phases 1 and 3, at the upper and lower wingstroke turning points. By contrast, the swift-generated wake circulations vary more gradually, and the negative peak is not at the lower turning point, but in mid-upstroke, at phase 2. These studies are based on far-wake data only and so the mechanisms underlying the continuous shedding of spanwise vorticity in the swift cannot easily be traced back to the local wing motions or aerodynamics. There could be continuous changes in several concomitant or isolated properties such as local angle of attack, camber, wing section geometry and/or relative velocity. However, the contrast between the two species in

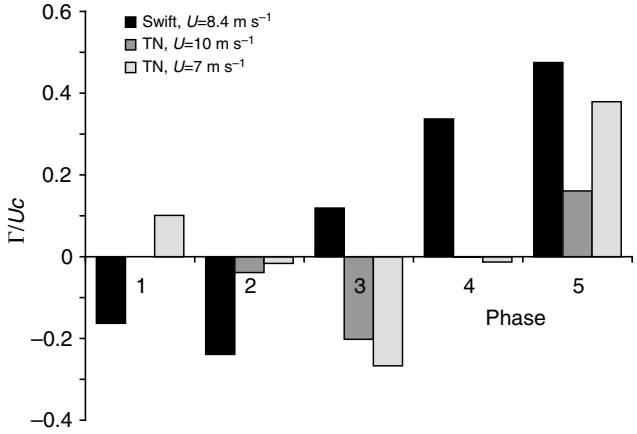

Fig. 9. The variation in normalized circulation over the five wingbeat phases for the swift and for the thrush nightingale (TN) at two flight speeds, U=7 and 10 m s^{-1}, that describe medium- and high-speed flight, respectively, in wind tunnel conditions. The swift data come from Fig. 7A and the thrush nightingale data from the database described in Spedding et al. (Spedding et al., 2003b). The data from both species come from the inner wing.

Fig. 10. Three-dimensional wake structure of the swift in cruising flight. The image frame is as if the bird flew obliquely from right to left and slightly into the paper, leaving the trace of one wingbeat in still air, starting at the upper turning point. Green tubes show the wingtip vortices, cylinders in shades of red are spanwise vortices with positive circulation and cylinders in shades of blue have negative circulation. The colour intensities and tube diameters are proportional to the strengths of each component. The geometry is deduced from a combination of wingbeat kinematics and streamwise plane section data.

Fig. 9 is consistent with larger amplitude variations in wings that flex significantly during the upstroke.

Insects also fly with comparatively rigid wings, having no distal joints or articulations, although passive elastic deformation makes them significantly non-planar. The wake of a hawkmoth (*Manduca sexta*) has certain characteristics similar to those of previously studied passerines such as the thrush nightingale, with intermediate wake formations between isolated vortex loops and constant circulation wakes (Bomphrey, 2006). The composite wake of the hawkmoth flying at 3.5 m s^{-1} shows continuous shedding of spanwise vorticity but, unlike the swift, both the down- and upstroke generate a mix of positive and negative vorticity. Furthermore, a part of the hawkmoth wake appears to form a distinct vortex loop (Bomphrey et al., 2006), which is not found in the swift wake.

A schematic summary of the three-dimensional swift wake topology is given in Fig. 10. The picture is a somewhat stylized summary of information from qualitative and quantitative spanwise vorticity distributions at different locations along the wing, combined with the measured kinematics. Cylinders in hues of red denote positive circulation and cylinders in hues of blue represent negative circulation. The distribution of the circulation intensity is based on data in Fig. 7. The green trailing, streamwise vortices are drawn by inference from figures such as Fig. 5.

Force balance

The continuous shedding of spanwise vortices illustrated in Fig. 10 cannot be adequately modelled by discrete vortex loop models derived either from the power-glider or from a pulsed ring generator, so neither reference circulations Γ_0 or Γ_1 are very useful (Fig. 8). Here we present an empirical model that integrates the accumulated wake circulation changes over the wingspan and over one wake wavelength. The completeness of the modelling effort can then be checked by comparing the calculated integrated vertical force with the known weight of the swift.

The continuous change model

The measured wake contains a time history of the circulation changes on the wing. In order to calculate the total integrated circulation we must add one further assumption about the absolute circulation value at some point. As a starting estimate, we shall assume that the circulation falls to zero at the end of the upstroke. This is a consistent interpretation of the very weak vorticity in phases 1 and 5 in Fig. 4, but others are possible and we must await further support from the force balance calculation itself. The net circulation (positive minus the absolute value of negative) found in each phase from the beginning of the downstroke to the end of the upstroke can be added to derive the accumulated circulation in the bound vortex and subsequently the vertical and horizontal impulse.

The measured wake circulations have been discretized at four spanwise locations and over five time intervals or wake phases (as shown in Fig. 7, for example). At the *j*th spanwise location, a local span section of width b_j can be identified, and then the vertical impulse, I_z, for that segment, over the phases comprising the downstroke part of the wake is:

$$I_{z,\mathrm{d},j} = \rho 2 b_j \frac{\lambda}{5}\left(\Gamma_5 + \Gamma_4 + \frac{\Gamma_3}{2}\right), \tag{6}$$

where the *j* indices are LR, X, Y, Z for the locations noted in Fig. 2. The local span-lengths, b_j, are measured from the centreline out to the wingtip. Each phase of the wake covers 1/5th of its wavelength λ, and Γ_5 to Γ_3 are the total accumulated circulations in phases 5 to 3, proceeding in order from the beginning of the downstroke to the lower turning point. Γ_3 marks the transition from downstroke to upstroke and appears also in the equivalent calculation of the upstroke wake impulse:

$$I_{z,\mathrm{u},j} = \rho 2 b_j R \frac{\lambda}{5}\left(\frac{\Gamma_3}{2} + \Gamma_2 + \Gamma_1\right). \tag{7}$$

The upstroke spans are reduced uniformly by the span ratio, *R*. If a more detailed, localized, accounting of the wing flexion were required, then it could be written directly into specific values for b_j, or into localized corrections, R_j.

The calculation includes the circulation contribution from the body wake (Fig. 7D), whose vortex wake signature is not easily extracted from that of the wing root. However, even though the wake vortices are as strong, or stronger than their counterparts further out on the wing, their net effect is approximately zero because there are equal amounts of positively and negatively signed vorticity. If the circulation increment is instead calculated from interpolating the LX and RX components across the body, the numerical result is the same within the calculation uncertainty.

Now the total impulse of a wake tiled by rectangular elements ($I_{z,\mathrm{rect}}$) of area $b_j(\lambda/5)$ (or $b_j(\lambda/5)R$ for the upstroke) is the sum of the downstroke and upstroke components over all span stations:

$$I_{z,\mathrm{rect}} = \sum_j \left(I_{z,\mathrm{d},j} + I_{z,\mathrm{u},j}\right), \quad j \in \{\mathrm{LR,X,Y,Z}\}. \tag{8}$$

The wake geometry is better approximated by elliptical shapes on both the down- and upstroke (Fig. 11), and so the wake area, and its impulse, should be modified by the area ratio of an ellipse to a rectangle, which is $\pi/4$. Since we use the wingspan as a measure of wake width (rather than the wake measurements themselves, which are too sparsely distributed in the spanwise direction) then an improved measure of the actual width for an elliptically loaded wing is $2b(\pi/4)$ (Milne-Thompson, 1966) and so the final total vertical impulse is:

$$I_z = \frac{\pi^2}{16} I_{z,\mathrm{rect}}. \tag{9}$$

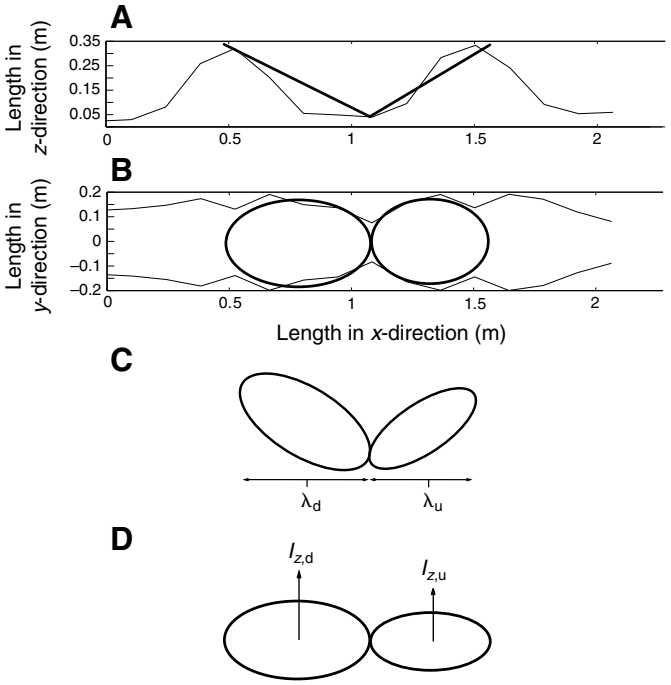

Fig. 11. Approximating the wake shape by ellipses. Flight direction is from right to left, and wingtip traces are viewed from the side (A) and above (B). Heavy lines denote ellipses fitted to the down- and upstroke wake geometry. The ellipses are seen from above in B and obliquely from the side in C, and their projection onto the horizontal plane is shown in D.

Substituting measured wake circulation values yields I_z=0.047 Ns. The uncertainty in estimating I_z is dominated by the uncertainty in Γ values. These form a population of repeated measurements of the same kind and so a total relative uncertainty in I_z can be estimated from the root mean square:

$$\frac{\Delta I_z}{I_z} = \left[\frac{1}{n_s n_p} \sum_{j=1}^{n_s} \sum_{i=1}^{n_p} \left(\frac{\Delta \Gamma_{i,j}}{\Gamma_{i,j}} \right)^2 \right]^{1/2}, \qquad (10)$$

where j is the same index over span stations {LR,X,Y,Z}, n_p=5 is the number of wingbeat phases and n_s=4 is the number of spanwise stations. $\Delta I_z/I_z$=0.3, and so the result for I_z can be written I_z=0.05±0.015 Ns (mean ± s.d.). In level, unaccelerated flight, I_z supports the weight W for a time T, and WT=0.044±0.003 Ns. Within experimental uncertainty WT=I_z and the wake-based calculation gives a result that is consistent with the observed experiment – that is, the bird flies level. Indirectly, therefore, the initial assumption that the circulation on the wing drops to zero at the end of the upstroke is also supported.

The approximate balance of forces implies, but does not prove, that vortex-induced flows measured in the wake are sufficient to explain the forces from the beating wing. As noted in the Introduction, additional terms could still be encountered from acceleration of the vortex elements themselves, leading to a contribution from the vortex added-mass. Dabiri (Dabiri, 2005) proposed a vortex–wake ratio, Wa, as a measure of the importance of flow unsteadiness when such terms might be important, with a corrected formulation in Dabiri et al. (Dabiri et al., 2006). Wa is proportional to the difference between the true convection of a vortex structure and its own self-induced velocity (the velocity it would have in the absence of external influences) and can be estimated from the wake data in experiments like these. Hedenström et al. (Hedenström et al., 2006b) estimated Wa for a thrush nightingale at its slowest flight speed of 4 m s^{-1}, when unsteady effects are most likely to be important, and found that Wa=0.06, about 7 times less than the suggested threshold criterion. In the swift wake, there are no strong, single coherent wake structures and no simple description of line vortices (such as rings) can be given. The unsteady, time-varying terms describing the wake evolution will be smaller still, and added mass terms can be ignored. Such is the case in the far wake described here, and we await further studies of the near-wake dynamics when the question can be re-examined.

The continuously varying wake circulation, and its implied continuous variation of loading on the wing itself points to a wing that generates thrust not by flexing greatly on the upstroke, but by reducing the local aerodynamic angle of attack. This rigid-wing wake, and the quite simple kinematics that produce it, make the numerical modelling much different from that of previously studied birds. The simple empirical integration model presented here is self-consistent and suggests that a more sophisticated wake model with constantly varying spanwise and streamwise vorticity, somewhat analogous to Prandtl's horseshoe vortex model (Prandtl and Tietjens, 1934) but following a slowly varying wing path, could be successful too. The unsteady lifting-line model of Phlips et al. (Phlips et al., 1981) has a prescribed wake geometry that is quite similar to that assumed here, as does that of Hall et al. (Hall et al., 1997), where the wake geometry is that produced by the time-varying wing circulation distribution, which minimizes the power consumption. The wakes in both studies are qualitatively similar to the one modelled here (Figs 10, 11), partly because the swift wing is relatively rigid.

Hall et al. (Hall et al., 1997) predicted a trade-off between flapping amplitude and flapping frequency, with a ridge of optimum power requirements from amplitudes θ_h=35° at k_b=4 to θ_h=20° at k_b=10, where θ_h=(θ_u + θ_d)/2 and k_b is a reduced frequency based on span, reading:

$$k_b = \frac{\omega 2b}{U},$$

in our notation. However, k_b for the swift never reaches the values predicted by Hall et al., varying from 2.2 to 2.7. Flapping amplitudes are also significantly higher, with $\theta_h \approx 55°$ being typical, and the model does not predict the kinematics observed here. Phlips et al. (Phlips et al., 1981) did not perform an optimization study but investigated the propulsive efficiency while varying independent parameters prescribed by a particular kinematics/wake. They also describe a balance between flapping amplitude and frequency, and reported that time-averaged unsteady effects were only beneficial when the equivalent frequency parameter kb>2. While this criterion is met by the swifts, the modelling effect of collecting together vortex elements at the extremes of the wingbeat, we now see, is not supported by the data.

In both cases, further quantitative progress might depend more on the correct modelling of viscous terms, most particularly the drag on the wings and body, which is difficult to measure and predict even for steady wings at this Reynolds number, Re (Spedding et al., 2008).

Estimating drag and L/D ratio

The measurement of wing and body drag in animal flight is notoriously difficult, and the sensible outcome of the model with respect to weight support encourages its extension to the estimation of horizontal forces from the wake properties, as in Hedenström et

al. (Hedenström et al., 2006a). Let us suppose that the identified wake structure (Fig. 4A–C) accounted for in the calculations above is distinct from the drag wakes that also must be present (i.e. Fig. 4D, Fig. 6). Projecting the ellipses of down- and upstroke (Fig. 11) onto the vertical (rather than horizontal) plane yields the impulse directed in the horizontal direction, analogous to Eqns 6 and 7, as:

$$I_{x,\mathrm{d},j} = \rho 2 b_j \frac{A}{5}\left(\Gamma_5 + \Gamma_4 + \frac{\Gamma_3}{2}\right), \quad (11)$$

and

$$I_{x,\mathrm{u},j} = \rho 2 b_j R \frac{A}{5}\left(\frac{\Gamma_3}{2} + \Gamma_2 + \Gamma_1\right), \quad (12)$$

for the downstroke and upstroke, respectively, where A is the wingbeat amplitude. The net horizontal impulse, defined as positive in the direction of flight, comes from the difference between the down- and upstroke components over all span locations:

$$I_{x,\mathrm{rect}} = \sum_j (I_{x,\mathrm{d},j} - I_{x,\mathrm{u},j}), \quad j \in \{\mathrm{LR,X,Y,Z}\}. \quad (13)$$

The same correction is made for wake shape and span efficiency, and so the net horizontal force is:

$$F_x = \frac{I_x}{T} = \frac{\pi^2}{16}\frac{I_{x,\mathrm{rect}}}{T}. \quad (14)$$

Since flight speed is constant, the net forward force is equal and opposite to the total drag, D, on the wings and body.

In steady horizontal motion there is no net horizontal momentum in the wake, and the local velocity defects caused by friction and pressure drag on the wings and body will be exactly balanced by the net thrust. In making analytical models (e.g. Rayner 1979a; Phlips et al., 1981; Spedding, 1987) it is common to construct a wake composed of relatively few vortex elements and to suppose that the net forward momentum flux in this wake balances the viscous drag, which itself is not explicitly modelled. Similarly, one might imagine that the simple wake models derived from experiments such as these represent the thrust wake generated by the wings, but not the drag component. As a very simple example, Fig. 10 and Eqns 11–14 do not include the observed body drag wake patterns seen in Fig. 6A. Note that Eqns 11 and 12 use amplitudes from kinematics and not from the observed wake geometry. The latter could be used but are known with less certainty as the self-induced wake deformations would complicate simple geometric measures. The idea that the identified wake structure corresponds to a pattern that balances a separate drag component is plausible but difficult to test because accounting for all components of the wake would require tracing their origin back to particular events on the wings and body.

Making the assumption above, Eqn 14 can now be used to calculate the drag of the whole bird in flight, and for the swift this value is $D=F_x=0.029$ N. In steady flight, the lift, L, is equal to the weight, $L=W=0.383$ N, and so at a flight speed $U=8.4$ m s^{-1}, the effective $L/D=13.3$.

A similar approach (with the same assumptions) gave $L/D=7.5$ for a robin in flapping flight at 9 m s^{-1} (Hedenström et al., 2006a). The higher L/D for the swift suggests that the aerodynamic design of the swift is better optimized for energy-efficient flight, and the streamlined body and the high aspect ratio wings are obvious morphological indicators that would make such a finding unsurprising. The L/D estimate applies only to the specific flight speed for which it is measured, and even though the bird was allowed to fly at its preferred flight speed, this does not necessarily correspond to the maximum L/D. Further, we may note that L/D for flapping flight is not obviously related to the same quantity for gliding flight. Due to the flapping motion, both extra lift and extra drag are expected, but their relative change is not known. Previous estimates of L/D in gliding flight are 12.6 for a jackdaw (Rosén and Hedenström, 2001) and 10.9 for a Harris' hawk (Tucker and Heine, 1990). These birds both have less streamlined bodies and lower aspect ratio wings than the swift but have almost as high an L/D in gliding as does the swift in flapping flight. L/D for the gliding swift may yet be higher still, and DPIV studies of the steady gliding flight of swifts are planned. Lentink et al. (Lentink et al., 2007) measured the lift and drag forces of preserved swift wings with varying sweep and at different airspeeds, and L/D of the swift wing–body assembly was approximately equal to 10 at $U=9$ m s^{-1}. L/D at each fixed sweep angle was a very sensitive function of flight speed. Although care was taken to allow passive deformation in response to the aerodynamic loading, working with inanimate animal parts is always problematic and the higher measurement from flapping flight suggests that the free gliding value could rather be higher still.

Based on the same assumptions as for the L/D estimate, one may also define time-averaged lift and drag coefficients for the entire wing/body assembly as:

$$C_\mathrm{L} = \frac{L}{qS}, \quad C_\mathrm{D} = \frac{D}{qS}, \quad (15)$$

where $q=\rho U^2/2$ is the dynamic pressure and S is the wing planform area (given in Table 1). The required/measured $C_\mathrm{L}=0.61$, which is readily obtained in well-designed wings at these Reynolds numbers ($Re=Uc/\nu$, where c is the mean chord length and ν is the kinematic viscosity; for $U=8.4$ m s^{-1}, $Re=2.2\times10^4$) but higher than the value of approximately 0.4 inferred from wake measurements of other species flying close to their preferred flight speed (Spedding et al., 2008). Defined as above, $C_\mathrm{D}=0.05$. Caution is required in comparing C_D values because the reference area must (1) be specified precisely, and (2) be the same between cases. Here we use wing planform area simply for convenience. Alternatives include total wetted surface area and projected frontal surface area, neither of which is readily calculated from the data available. The Lentink et al. (Lentink et al., 2007) experiments measured lift:drag polars of pairs of fixed swift wings glued together, calculated a drag coefficient from the force balance measurements and then added a drag coefficient for the body. Since the wing calculation used S as the reference area, the measurements are roughly comparable to those given here. The wing pairs occupied a family of lift:drag polars with varying sweep angle, and for the $C_\mathrm{L}=0.6$ calculated here, values of C_D ranged from 0.045–0.08. Our value of 0.05 lies at the lower end of the range, even though it was calculated for flapping flight.

Cost and benefit of the flight style

During downstroke the forward force is $I_{x,\mathrm{d}}/T=0.07$ N and during the upstroke the opposite force is $I_{x,\mathrm{u}}/T=0.04$ N. Thus, the counteracting negative thrust during the upstroke is approximately 60% of the thrust generated during the downstroke, implying that the active upstroke is expensive from a thrust generation point of view. However, similar calculations show that the lift produced during the upstroke is also 60% of that produced during the downstroke. This relatively high upstroke contribution to the lift

may be why the active upstroke is favoured despite the cost in reduced thrust. Moreover, there could be benefits in control and manoeuvrability if a large part of the wing is always active, and agility may well be as important in the ecological balance as steady flight efficiency.

CONCLUDING REMARKS

Swifts are renowned for their extreme aerial lifestyle, and also for their curved, relatively inflexible wings. The lunate planform has been shown to be efficient in analytical models of unsteady, low amplitude propulsion (Lighthill, 1970; Cheng and Murillo, 1984; Karpouzian et al., 1990), originally applied to bony fish, sharks, whales and dolphins. The rigidity of the wings may indicate an attempt to maintain this efficient shape in straight and turning flight. Because the wings do not flex on the upstroke as in many other birds of comparable size, their wakes are different too, reflecting an upstroke that seems to be a slightly feathered (local incidence angles on the wing are reduced to reduce the magnitude of the forces) version of the downstroke.

The almost continuous shedding of spanwise vorticity into the wake is very different from that of birds studied thus far, and requires a different empirical model of the vortex wake. The simple integration of the wake components presented here appears to be successful in accounting for the gross, time-averaged forces in steady flight. Although it is still difficult to deduce wing properties from these far-wake measurements, the estimated effective L/D=13.3 is quite respectable for flapping flight at these Reynolds numbers, and is higher than yet measured for any other live bird.

The variation of local wing loading by variation in local angle of attack of a comparatively rigid wing is much more similar to something that might be emulated when constructing a micro air vehicle (MAV), where excess flexibility can lead to prediction and resonance problems (e.g. Shyy et al., 1999; Lian and Shyy, 2007). Not only is the basic mechanical design easier but also the reduced amplitude of variation of the aerodynamic forces leads to much easier design for stable flight. MAV-sized ornithopters may be more swift-like than any other bird studied so far.

LIST OF ABBREVIATIONS AND SYMBOLS

A	wingbeat amplitude
b	wing semispan
b_j	width of local span section
c	mean wing chord
C_D	coefficient of drag
C_L	coefficient of lift
D	drag force
f	wingbeat frequency
$\boldsymbol{g}$	gravitational acceleration
I_x	horizontal wake impulse
I_z	vertical wake impulse
L	lift force
m	mass of the bird
q	dynamic pressure
R	span ratio
S	wing area
S_e	projected area of wake ellipse
T	wingbeat period
T_d	downstroke duration
U	flight speed
W	body weight
Γ	circulation
Γ_0	reference circulation for weight support in steady gliding flight
Γ_1	reference circulation for weight support by downstroke vortex loop
θ	stroke angle
λ	wake wavelength
ρ	air density

Subscripts u and d indicate upstroke and downstroke, respectively.

We are grateful to Jan Holmgren for providing the two juvenile swifts and for support during this project. We also wish to thank Hilde Matthes for instructions on the technique of hand feeding swifts and Erich and Gertrud Kaiser for information about swifts in general. We thank Teresa Kullberg for excellent help during the experiments and our colleagues Florian Muijres, Christoffer Johansson and Marta Wolf for ideas and suggestions along the way of this project, and finally Mikael Rosén for his part in collecting the thrush nightingale data. This study was financially supported by grants from the Swedish Research Council, the Swedish Foundation for International Cooperation in Research and Higher Education and the Knut and Alice Wallenberg Foundation. A.H. is a Royal Swedish Academy of Science Research Fellow supported by grants from the Knut and Alice Wallenberg Foundation.

REFERENCES

Bäckman, J. and Alerstam, T. (2001). Confronting the winds: orientation and flight behaviour of the roosting swift, *Apus apus*. *Proc. R. Soc. Lond. B Biol. Sci.* **268**, 1081-1087.
Bäckman, J. and Alerstam, T. (2002). Harmonic oscillatory orientation relative to the wind in nocturnal roosting flights of the swift *Apus apus*. *J. Exp. Biol.* **205**, 905-910.
Bomphrey, R. J. (2006). Insects in flight: direct visualization and flow measurements. *Bioinspir. Biomim.* **1**, S1-S9.
Bomphrey, R. J., Lawson, N. J., Taylor, G. K. and Thomas, A. L. R. (2006). Application of digital particle image velocimetry to insect aerodynamics: measurements or the leading-edge vortex and near wake of a Hawkmoth. *Exp. Fluids* **40**, 546-554.
Bruderer, B. and Weitnauer, E. (1972). Radarbeobachtungen über Zug und Nachtflüge des Mauerseglers (*Apus apus*). *Rev. Suisse Zool.* **79**, 1190-1200.
Cheng, H. K. and Murillo, L. (1984). Lunate-tail swimming propulsion as a problem of curved lifting line in unsteady flow. Part 1. Asymptotic theory. *J. Fluid Mech.* **143**, 327-350.
Dabiri, J. O. (2005). On the estimation of swimming and flying forces from wake measurements. *J. Exp. Biol.* **208**, 3519-3532.
Dabiri, J. O., Colin, S. P. and Costello, J. H. (2006). Fast-swimming hydromedusae exploit velar kinematics to form an optimal vortex wake. *J. Exp. Biol.* **209**, 2025-2033.
Hall, K. C., Pigott, S. A. and Hall, S. R. (1997). Power requirements for large-amplitude flapping flight. AIAA 1997-0827, http://www.aiaa.org.
Hedenström, A., Rosén, M. and Spedding, G. R. (2006a). Vortex wakes generated by robins *Erithacus rubecula* during free flight in a wind tunnel. *J. R. Soc. Interface* **3**, 263-276.
Hedenström, A., van Griethuijsen, L., Rosén, M. and Spedding, G. R. (2006b). Vortex wakes of birds: recent developments using digital particle image velocimetry in a wind tunnel. *Anim. Biol.* **56**, 535-549.
Hedenström, A., Johansson, L. C., Wolf, M., von Busse, R., Winter, Y. and Spedding, G. R. (2007). Bat flight generates complex aerodynamic tracks. *Science* **316**, 894-897.
Holmgren, J. (2004). Roosting in tree foliage by Common Swifts *Apus apus*. *Ibis* **146**, 404-416.
Karpouzian, G., Spedding, G. R. and Cheng, H. K. (1990). Lunate-tail swimming propulsion. Part 2. Performance analysis. *J. Fluid Mech.* **210**, 329-351.
Kokshaysky, N. V. (1979). Tracing the wake of a flying bird. *Nature* **279**, 146-148.
Lack, D. (1956). *Swifts in a Tower*. London: Methuen.
Lentink, D., Müller, U. K., Stamhuis, E. J., de Kat, R., van Gestel, W., Veldhuis, L. L. M., Henningsson, P., Hedenström, A., Videler, J. J. and van Leeuwen, J. L. (2007). How swifts control their glide performance with morphing wings. *Nature* **446**, 1082-1085.
Lian, Y. and Shyy, W. (2007). Laminar-turbulent transition of a low Reynolds number rigid or flexible airfoil. *AIAA J.* **45**, 1501-1513.
Lighthill, M. J. (1970). Aquatic animal propulsion of high hydromechanical efficiency. *J. Fluid Mech.* **44**, 265-301.
Milne-Thompson, L. M. (1966). *Theoretical Aerodynamics*. New York: Dover.
Park, K. J., Rosén, M. and Hedenström, A. (2001). Flight kinematics of the barn swallow *Hirundo rustica* over a wide range of speeds in a wind tunnel. *J. Exp. Biol.* **204**, 2741-2750.
Peng, J. and Dabiri, J. O. (2008). An overview of a Lagrangian method for analysis of animal wake dynamics. *J. Exp. Biol.* **211**, 280-287.
Pennycuick, C. J. (1988). On the reconstruction of pterosaurs and their flight manner, with notes on vortex wakes. *Biol. Rev.* **63**, 299-331.
Pennycuick, C. J. (1989). *Bird Flight Performance: A Practical Calculation Manual*. Oxford: Oxford University Press.
Pennycuick, C. J. (1996). Wingbeat frequency of birds in steady cruising flight: new data and improved predictions. *J. Exp. Biol.* **199**, 1613-1618.
Pennycuick, C. J., Alerstam, T. and Hedenström, A. (1997). A new low-turbulence wind tunnel for bird flight experiments at Lund University, Sweden. *J. Exp. Biol.* **200**, 1441-1449.
Phlips, P. J., East, R. A. and Pratt, N. H. (1981). An unsteady lifting line theory of flapping wings with application to the forward flight of birds. *J. Fluid Mech.* **112**, 97-125.
Prandtl, L. and Tietjens, O. G. (1934). *Fundamentals of Hydro- and Aeromechanics*. New York: Dover.
Rayner, J. M. V. (1979a). A vortex theory of animal flight. I. The vortex wake of a hovering animal. *J. Fluid Mech.* **91**, 697-730.

Rayner, J. M. V. (1979b). A vortex theory of animal flight. II. The forward flight of birds. *J. Fluid Mech.* **91**, 731-763.
Rayner, J. M. V. (1979c). A new approach to animal flight mechanics. *J. Exp. Biol.* **80**, 7-54.
Rayner, J. M. V., Jones, G. and Thomas, A. (1986). Vortex flow visualization reveal change in upstroke function with flight speed in bats. *Nature* **321**, 162-164.
Rosén, M. and Hedenström, A. (2001). Gliding flight in a jackdaw: a wind tunnel study. *J. Exp. Biol.* **204**, 1153-1166.
Rosén, M., Spedding, G. R. and Hedenström, A. (2004). The relationship between wingbeat kinematics and vortex wake of a thrush nightingale. *J. Exp. Biol.* **207**, 4255-4268.
Rosén, M., Spedding, G. R. and Hedenström, A. (2007). Wake structure and wingbeat kinematics of a house-martin *Delichon urbica*. *J. R. Soc. Interface* **4**, 659-668.
Shyy, W., Berg, M. and Ljungquist, D. (1999). Flapping and flexible wings for biological and micro air vehicles. *Prog. Aerosp. Sci.* **35**, 455-505.
Spedding, G. R. (1986). The wake of a jackdaw (*Corvus monedula*) in slow flight. *J. Exp. Biol.* **125**, 287-307.
Spedding, G. R. (1987). The wake of a kestrel (*Falco tinnunculus*) in flapping flight. *J. Exp. Biol.* **127**, 59-78.
Spedding, G. R., Rayner, J. M. V. and Pennycuick, C. J. (1984). Momentum and energy in the wake of a pigeon (*Columba livia*) in slow flight. *J. Exp. Biol.* **111**, 81-102.
Spedding, G. R., Hedenström, A. and Rosén, M. (2003a). Quantitative studies of the wakes of freely flying birds in a low-turbulence wind tunnel. *Exp. Fluids* **34**, 291-303.
Spedding, G. R., Rosén, M. and Hedenström, A. (2003b). A family of vortex wakes generated by a thrush nightingale in free flight in a wind tunnel over its entire natural range of flight speeds. *J. Exp. Biol.* **206**, 2313-2344.
Spedding, G. R., Hedenström, A., McArthur, J. and Rosén, M. (2008). The implications of low-speed fixed-wing aerofoil measurements on the analysis and performance of flapping bird wings. *J. Exp. Biol.* **211**, 215-223.
Tobalske, B. W., Hedrick, T. L. and Biewener, A. A. (2003). Wing kinematics of avian flight across speeds. *J. Avian Biol.* **34**, 177-184.
Tobalske, B. W., Warrick, D. R., Clark, C. J., Powers, D. R., Hedrick, T. L., Hyder, G. A. and Biewener, A. (2007). Three-dimensional kinematics of hummingbird flight. *J. Exp. Biol.* **210**, 2368-2382.
Tucker, V. A. and Heine, C. (1990). Aerodynamics of gliding flight in a Harris' hawk, *Parabuteo unicinctus*. *J. Exp. Biol.* **149**, 469-489.